

RESEARCH

Open Access



Atom-precise fluorescent copper cluster for tumor microenvironment targeting and transient chemodynamic cancer therapy

Zhenzhen Yang^{1†}, Anli Yang^{3†}, Wang Ma¹, Kai Ma², Ya-Kun Lv², Peng Peng^{1,2*}, Shuang-Quan Zang^{2*} and Bingjie Li^{1,2*} 

Abstract

Background: Reactive oxygen species (ROS) have been widely studied for cancer therapy. Nevertheless, instability and aspecific damages to cellular biomolecules limit the application effect. Recently, significant research efforts have been witnessed in the flourishing area of metal nanoclusters (NCs) with atomically precise structures for targeted release of ROS but few achieved success towards targeting tumor microenvironment.

Results: In this work, we reported an atomically precise nanocluster $\text{Cu}_6(\text{C}_4\text{H}_3\text{N}_2\text{S})_6$ (Cu_6NC), which could slowly break and generate ROS once encountered with acidic. The as-prepared Cu_6NC demonstrated high biological safety and efficient chemodynamic anti-tumor properties. Moreover, Cu_6NC enabled transient release of ROS and contained targeting behavior led by the tumor microenvironment. Both in vitro and in vivo experiments confirmed that Cu_6NC demonstrated a low cytotoxicity for normal cells, while presented high cytotoxicity for tumor cells with a concentration-dependent manner.

Conclusions: This work not only reported a promising candidate for chemodynamic cancer therapy, but also paved the route to address clinical issues at the atomic level.

Keywords: Nano clusters, Sustainable release, Targeting property, ROS, Cancer therapy

*Correspondence: ppeng@zzu.edu.cn; zangsqzg@zzu.edu.cn; bingjieli1991@outlook.com

[†]Zhenzhen Yang and Anli Yang contributed equally to this work

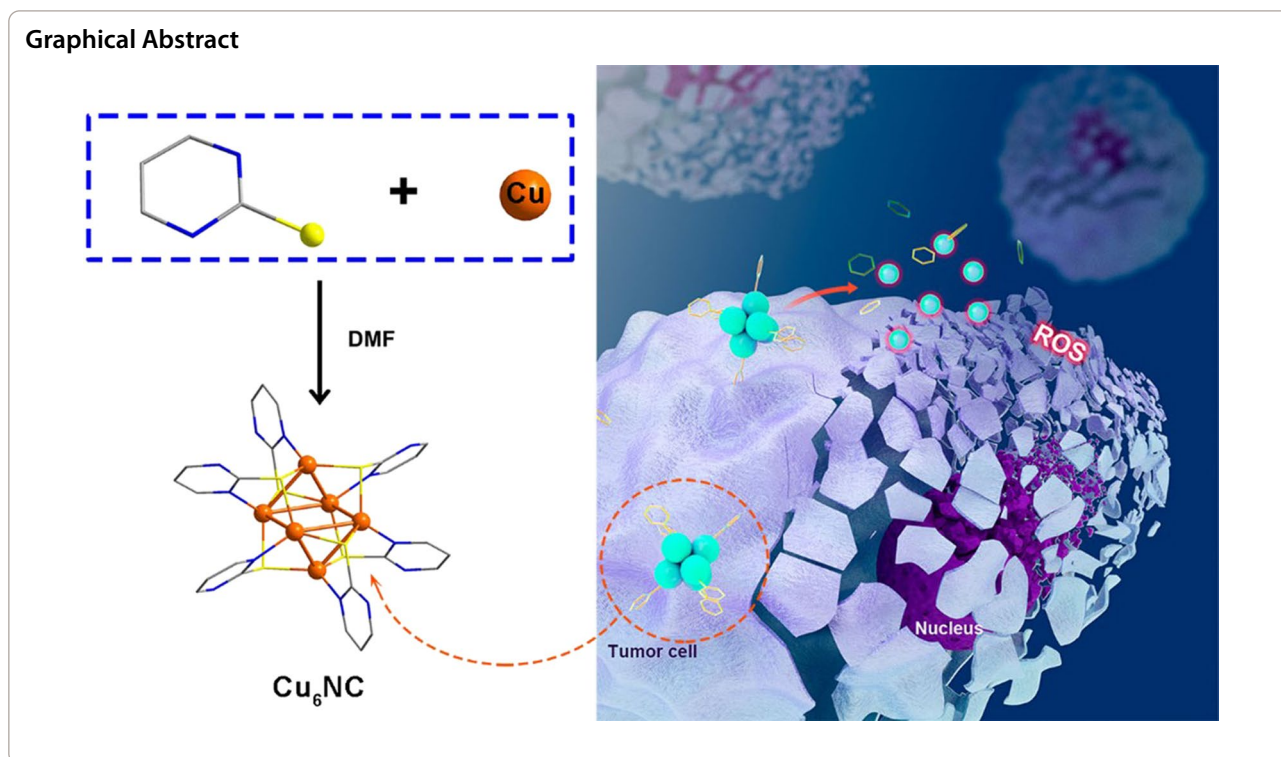
¹ Department of Oncology, The First Affiliated Hospital of Zhengzhou University, Zhengzhou 450052, China

² Henan Key Laboratory of Crystalline Molecular Functional Materials, Henan International Joint Laboratory of Tumor Theranostical Cluster Materials, Green Catalysis Center, and College of Chemistry, Zhengzhou University, Zhengzhou 450001, China

Full list of author information is available at the end of the article



© The Author(s) 2021. **Open Access** This article is licensed under a Creative Commons Attribution 4.0 International License, which permits use, sharing, adaptation, distribution and reproduction in any medium or format, as long as you give appropriate credit to the original author(s) and the source, provide a link to the Creative Commons licence, and indicate if changes were made. The images or other third party material in this article are included in the article's Creative Commons licence, unless indicated otherwise in a credit line to the material. If material is not included in the article's Creative Commons licence and your intended use is not permitted by statutory regulation or exceeds the permitted use, you will need to obtain permission directly from the copyright holder. To view a copy of this licence, visit <http://creativecommons.org/licenses/by/4.0/>. The Creative Commons Public Domain Dedication waiver (<http://creativecommons.org/publicdomain/zero/1.0/>) applies to the data made available in this article, unless otherwise stated in a credit line to the data.

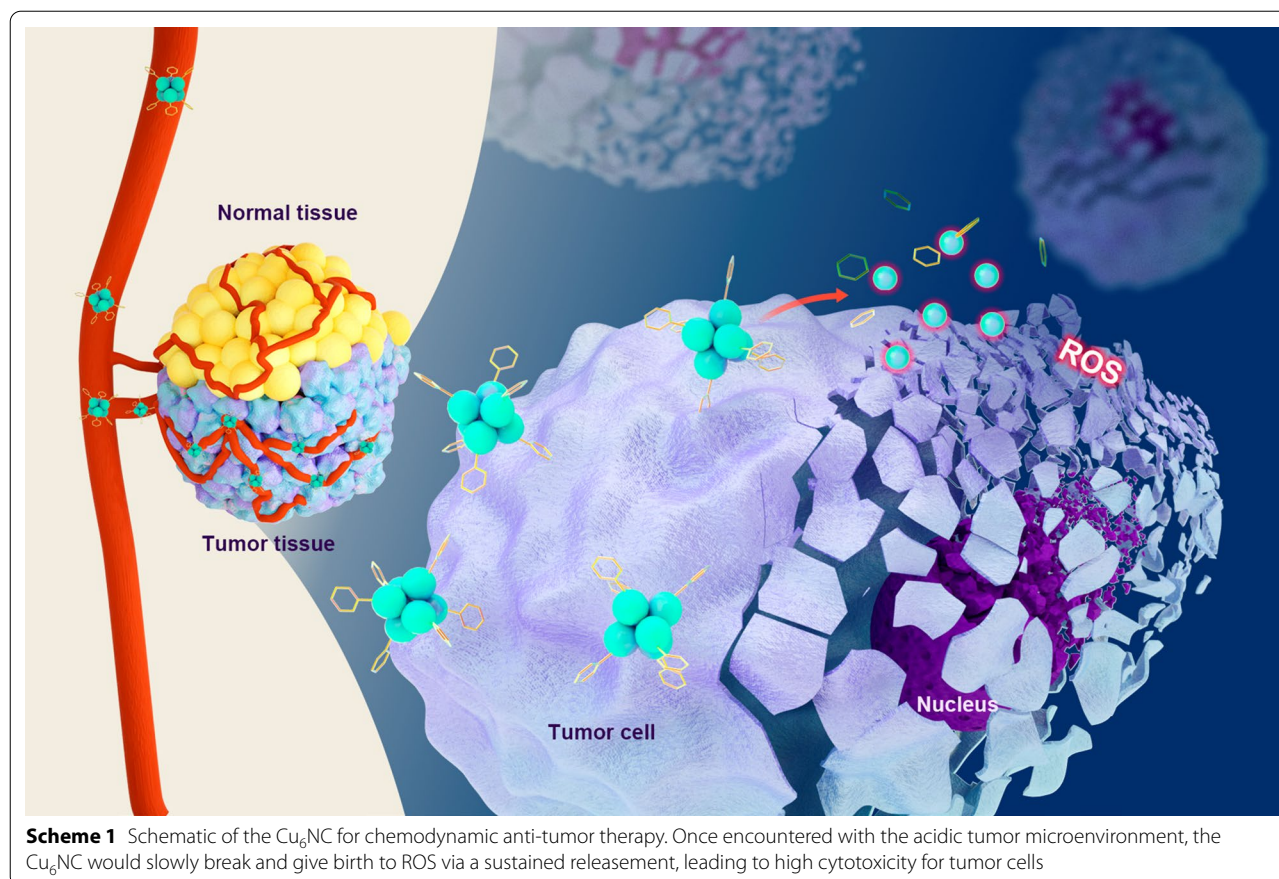


Introduction

Reactive oxygen species (ROS) are unstable molecules that contain oxygen, such as singlet oxygen, superoxide, hydroxyl radical and peroxide, etc. For the last decades, both experimental and clinical studies confirm that the alterations of ROS can affect the intracellular redox state [1–3]. Ever since, numerous efforts have been devoted to examine the role of ROS in cellular transformation and tumorigenesis [4, 5]. It has been observed that raising ROS level could effectively promote the apoptosis of cancer cells and modulate the immune response (specifically, inhibition) towards the treatment of cancer as well as autoimmune diseases [6–8]. Moreover, the elevation of ROS levels also contributes to tissue regeneration [9]. Many treatments such as the exposure of cancer cells to chemotherapy and radiotherapy could upregulate ROS [10–12]. Nevertheless, caused by the intrinsic instability, it is difficult for ROS to realize sustainable release for persistent anti-cancer effect. Meanwhile, a well-coordinated and balanced redox system is typically present under normal physiological conditions. Thus, promoting ROS may produce cellular stress and damage, since ROS can damage cellular biomolecules (such as proteins, DNA, RNA) and result in mutations or even carcinogenesis. Hence, the controllable presentation of ROS is vital to take advantage of this double-edged sword for cancer therapy.

Over the past decades, remarkable progress has been achieved in the area of nanomaterials such as atomically precise assembled nanoclusters [13–16]. Amongst the nanoclusters, atomically precise metal nanoclusters (NCs) has explored promising potentials with fine-tuned properties [17–19]. The bottom-up programmed assembly of these NCs make it relatively simple to control over the size and to replace the surface organic ligand, providing good opportunities for particular applications [20–24]. By far, various metal based NCs (especially gold) have demonstrated effective anti-cancer properties [25, 26]. For example, researchers have developed NCs that could make cancer cells more sensitive to radiation and promote the efficiency of radiotherapy [27–30]. Our previous work also explored photothermic behavior from coordinated-metal centers for cancer therapy [31]. By far, our group have designed and synthesized dozens of metal NCs with atomically precise assembly [32–38]. Benefiting from the precise formulas, both the structure and the physicochemical properties of atomically precise metal NCs are controllable [39, 40]. Thus, one could reasonably hypothesize that with rational design, the additional introduction of the organic ligand could modulate targeting properties while the functional modification may generate sustained releasement of NCs in particular position.

Herein, we reported an atomically precise nanocluster $\text{Cu}_6(\text{C}_4\text{H}_3\text{N}_2\text{S})_6$, which were determined by the single



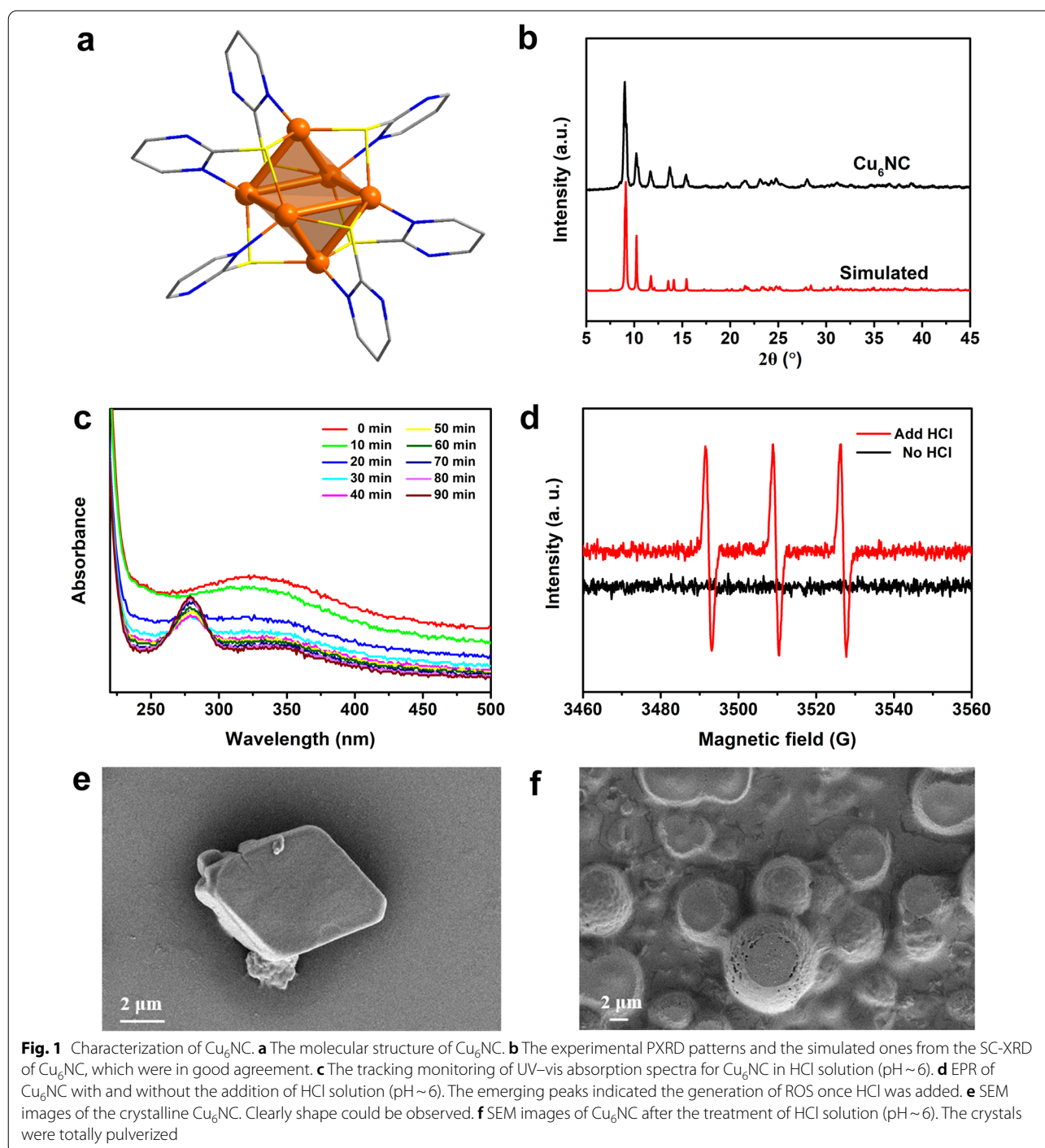
crystal X-ray diffraction (SC-XRD). 2-mercaptopyrimidine was used to assemble the precise structures and led to a size of ~ 1 nm of each cluster as calculated from the SC-XRD analysis. Consistently, none of cardiotoxicity, kidney toxicity or liver toxicity were observed in the main organs and peripheral blood, suggesting the good compatibility of our Cu_6NC . Specially, the structure $\text{Cu}_6(\text{C}_4\text{H}_3\text{N}_2\text{S})_6$ was quite stable unless mixed in acidic environment. The slight addition of acid ($\text{pH} \sim 6$) would slowly break the structure and generate the burst of radicals, realizing the sustained releasement of ROS (Scheme 1). The *in vitro* and *in vivo* experiments confirmed that Cu_6NC demonstrated a low cytotoxicity for normal cells, while presented high cytotoxicity for tumor cells with a concentration-dependent manner (Scheme 1). Such observations not only confirmed the biological safety and chemodynamic anti-tumor properties, but also indicated the targeting behavior led by the tumor microenvironment.

Results and discussions

Synthesis and characterization of $\text{Cu}_6(\text{C}_4\text{H}_3\text{N}_2\text{S})_6$ nanoclusters

Typically, the $\text{Cu}_6(\text{C}_4\text{H}_3\text{N}_2\text{S})_6$ nanocluster (Cu_6NC) was synthesized via one-pot route by blending

2-mercaptopyrimidine with $\text{Cu}(\text{NO}_3)_2 \cdot 3\text{H}_2\text{O}$ (ratio of 1/1 by mole) in dimethyl formamide (detailed in “Experimental section”). According to the SC-XRD analysis, each of the ligand bridges three Cu ions. Specially, each sulfur atom of the ligand bridges two Cu ions, while each Cu ion is coordinated with two sulfur atoms and one nitrogen atom from three independent ligands (Fig. 1a). The exact structure information could be found in the Additional file 1: Table S1. As shown in Fig. 1b, the experimental Powder-XRD (PXRD) patterns were in good agreement with the simulated ones from the SC-XRD, indicating the phase purity of the as-synthesized crystalline products of Cu_6NC . X-Ray photoelectron spectroscopy (XPS) (Additional file 1: Fig. S1a) confirmed that Cu_6NC contained C, N, S and Cu elements. The peaks at 932.6 and 952.5 eV in the high-resolution Cu 2p spectrum (Additional file 1: Fig. S1b) could be attributed to the $2p_{2/3}$ and $2p_{1/2}$ of Cu^+ , respectively [41, 42], which was generated by the reductive mercapto groups. In the Fourier transform infrared (FTIR) spectra (Additional file 1: Fig. S2), the adsorption peaks of S–H stretch were absent in the spectra of Cu_6NC and the C=C/C=N peaks were apparently red-shifted, suggesting the formation of the coordination



between mercaptopyrimidine and Cu ions [43]. Such coordinated ligands led to considerable thermal stabilities. Under nitrogen atmosphere, the thermogravimetric analysis (TGA) revealed that large weight loss (~40%) was observed at 400 °C, suggesting that Cu_6NC could be maintained from room temperature to nearly 400 °C (Additional file 1: Fig. S3).

Notably, Cu_6NC demonstrated crucial luminescent properties, indicating potential applications for biomedical labeling and targeting. The normalized emission spectra of the Cu_6NC showed long-wavelength emission bands of 700 nm (Additional file 1: Fig. S4), which was appealing for the biological test. Moreover, the fluorescence of Cu_6NC was reserved in water as well as in many

biological media (Additional file 1: Fig. S5), indicating that Cu₆NC held considerable stability for the potential biological applications. According to dynamic light scattering (DLS) analysis, the average size of Cu₆NC components in aqueous was ~23 nm (Additional file 1: Fig. S6), which was within the range enabling efficient uptake by tumors. Transmission electron microscopy (TEM) of the Cu₆NC (Additional file 1: Fig. S7) demonstrated a homogenous distribution with the size around 20 nm, which was smaller than the kidney filtration threshold. Moreover, obvious light absorption of Cu₆NC was observed at the wavelength of 370 nm during the solid state UV–vis absorption spectra test (Additional file 1: Fig. S8). Since the structure was quite stable in water, we further tracked the UV–vis absorption spectra curves of Cu₆NC in the HCl solution (pH ~6), observing a slowly structure changes (Fig. 1c). Meanwhile, the PXRD revealed that the crystalline structures of Cu₆NC were totally broken (Additional file 1: Fig. S9). More importantly, electron paramagnetic response (EPR) of Cu₆NC displayed significantly changed signals with the addition of HCl solution (pH ~6) (Fig. 1d), proving that a large number of ROS was produced. On the contrary, none signals was detected when tested the pure ligands under the same condition (Additional file 1: Fig. S10). The morphology analysis by scanning electron microscopy (SEM) and the associated energy dispersive spectroscopy (EDS) also revealed that the crystalline Cu₆NC with clear shape (Fig. 1e and Additional file 1: Fig. S11) was totally pulverized (Fig. 1f and Additional file 1: Fig. S12) after the treatment of acidic solution (pH ~6). This suggests that the slight addition of acid (pH ~6) would break the structure and generate the burst of radicals, realizing the release of ROS. We also performed the test of Fenton-like reactions with Cu₆NC in different pH, and the result showed that Fenton-like reactions were stronger in lower pH conditions, supporting our results that Cu₆NC can generate ROS under acid environment (Additional file 1: Fig. S13). The above results indicate that Cu₆NC maintains a stable structure in the simulated neutral normal tissue environment (pH ~7.4), and at the same time, rapidly dissociates and releases the inner core and generates ROS after entering the simulated acidic tumor microenvironment (pH ~6).

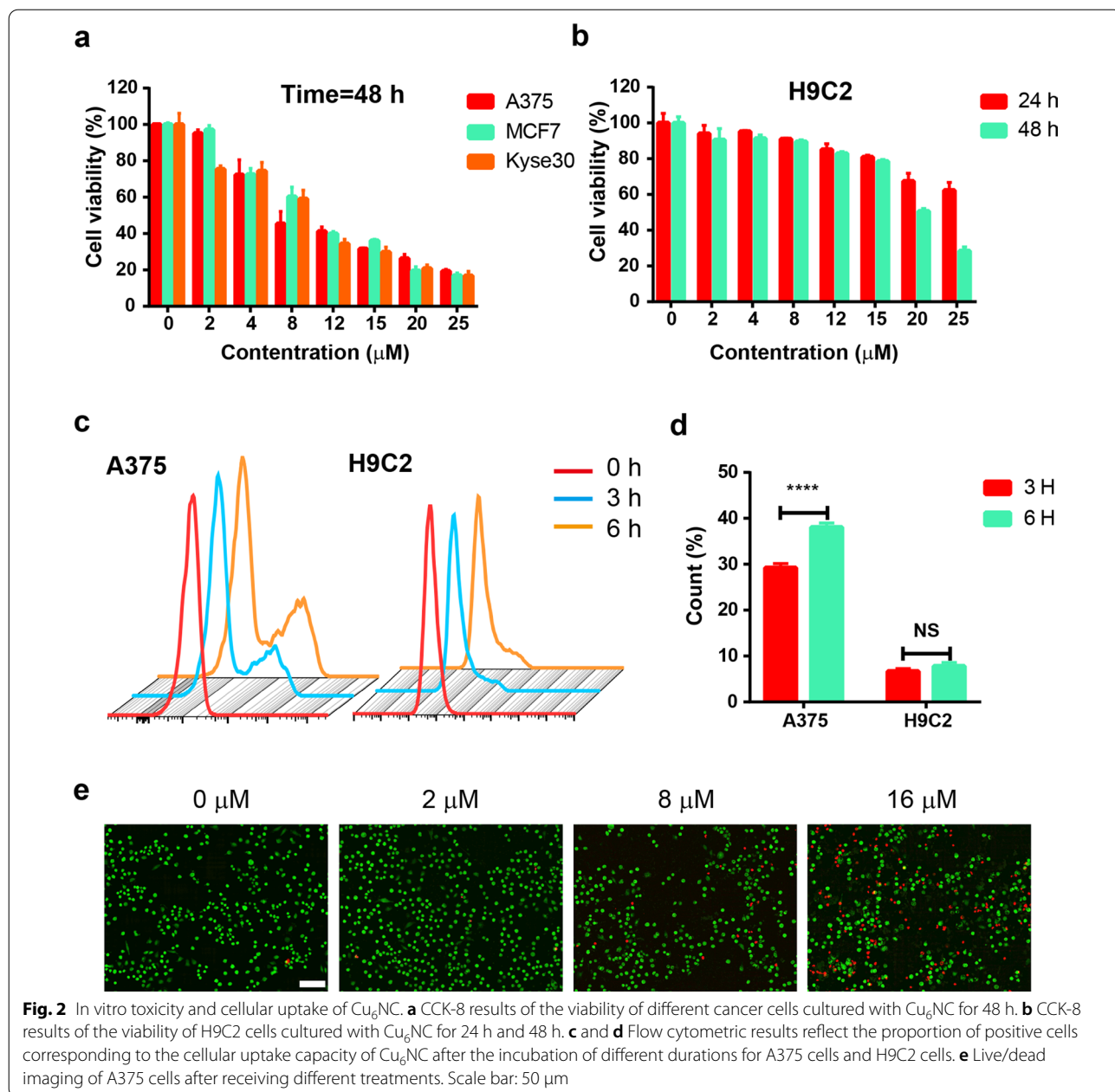
Cytotoxicity studies of Cu₆NC

The biological safety of Cu₆NC was evaluated by cell viability. Both normal (cardiomyocytes, H9C2) and cancer cell lines were used as models to assess cellular responses by CCK-8 assay kit. Cu₆NC demonstrated high cytotoxicity to tumor cells (Additional file 1: Fig. S14 and Fig. 2a). After treatment with 20 μM Cu₆NC for 48 h, the cell viability of A375, MCF-7 and Kyse30 cancer cell lines were

26.3%, 19.6%, and 20.9%, respectively (Fig. 2a). And its ligand components showed almost no effect on tumor cell viability (Additional file 1: Fig. S15). This is consistent with the EPR results (Fig. 1d and Additional file 1: Fig. S10), so we further confirmed the unique mechanism of Cu₆NC leading to cytotoxicity through structural fragmentation. On the contrary, low cytotoxicity was observed in normal cardiomyocytes for Cu₆NC (Fig. 2b). After 48 h of incubation, the inhibition rate of 20 μM Cu₆NC was only 49.3% and the cell viability was 78.5% at the 15 μM (administration level), which was much higher than that tumor cells at the same level. As we all know, compared with normal cells, tumor cells survive through more glycolytic pathways, which leads to an acidic microenvironment [44, 45]. The acid sensitivity of Cu₆NC is the main reason for its weak cytotoxicity to normal cells compared with tumor cells. Notably, we also measured the cellular uptake capacity of Cu₆NC into both A375 cells and normal cardiomyocytes (Fig. 2c, d) during flow cytometric test. Along with the increase of incubation durations, the proportion of positive cells was slightly raised in cardiomyocytes while obviously promoted in cancer cells. We speculated that tumor cells could attract more Cu₆NC during the instantaneous consumption of Cu₆NC, and the less reaction of Cu₆NC with cardiomyocytes determines the less cellular uptake. Therefore, we believed that the uptake of Cu₆NC was more effective in tumor cells. These phenomena confirmed that Cu₆NC was tumor-specific.

Investigations of anti-tumor properties

Due to the selective cytotoxic property, Cu₆NC was thoroughly evaluated for chemodynamic therapy (CDT) in vitro. The four groups of cells treated with different concentrations of Cu₆NC (0, 2, 8 and 16 μM) were analyzed. Subsequently, the apoptosis and cell cycle were evaluated by flow cytometry after 24 h. As shown in Fig. 3a and Additional file 1: Fig. S16, Cu₆NC promoted the apoptosis of A375 cells, thereby causing cell proliferation inhibition. Particularly, Cu₆NC could mediate cell arrest in G2 phase (Fig. 3b and Additional file 1: Fig. S17). Live/dead stain imaging showed more red fluorescence appeared with the increased concentration of Cu₆NC (Fig. 2e), suggesting that the viability of cells in the Cu₆NC decreased in a dose-dependent manner. Meanwhile, live/dead detection associated with flow cytometry (Additional file 1: Figs. S18 and S19) also demonstrated that after incubation with 0, 2, 8 and 16 μM Cu₆NC, the cell death rates were 3.63%, 7.14%, 23.0% and 42.2%, respectively. Since the formidable metastasis ability is one of the reasons that tumor cells are difficult to completely clean, we also performed transwell migration assay in vitro and observed that Cu₆NC could



significantly inhibit tumor cells migration (Fig. 3c and Additional file 1: Fig. S20). Furthermore, the cell colony formation assay was conducted to assess the chemodynamic efficacy of Cu_6NC over a longer period of time.

The corresponding results revealed similar dose-dependent (Fig. 3d and Additional file 1: Fig. S21). In the control group (0 μM), the colonies were densely packed and none effect on cell proliferation was observed. Specifically, the

(See figure on next page.)

Fig. 3 Chemokinetic anti-tumor properties of Cu_6NC . Cell flow cytometry analysis for apoptosis. **a** and cell cycle **b** distribution in A375 cells after different concentrations (0, 2, 8 and 16 μM) of Cu_6NC treatment. **c** Representative images of transwell migration assay. Scale bar: 50 μm . **d** Typical images representing the colony formation ability of A375 cells with different treatments. **e** ROS production in A375 cells after Cu_6NC treatment with different concentrations. Scale bar: 100 μm

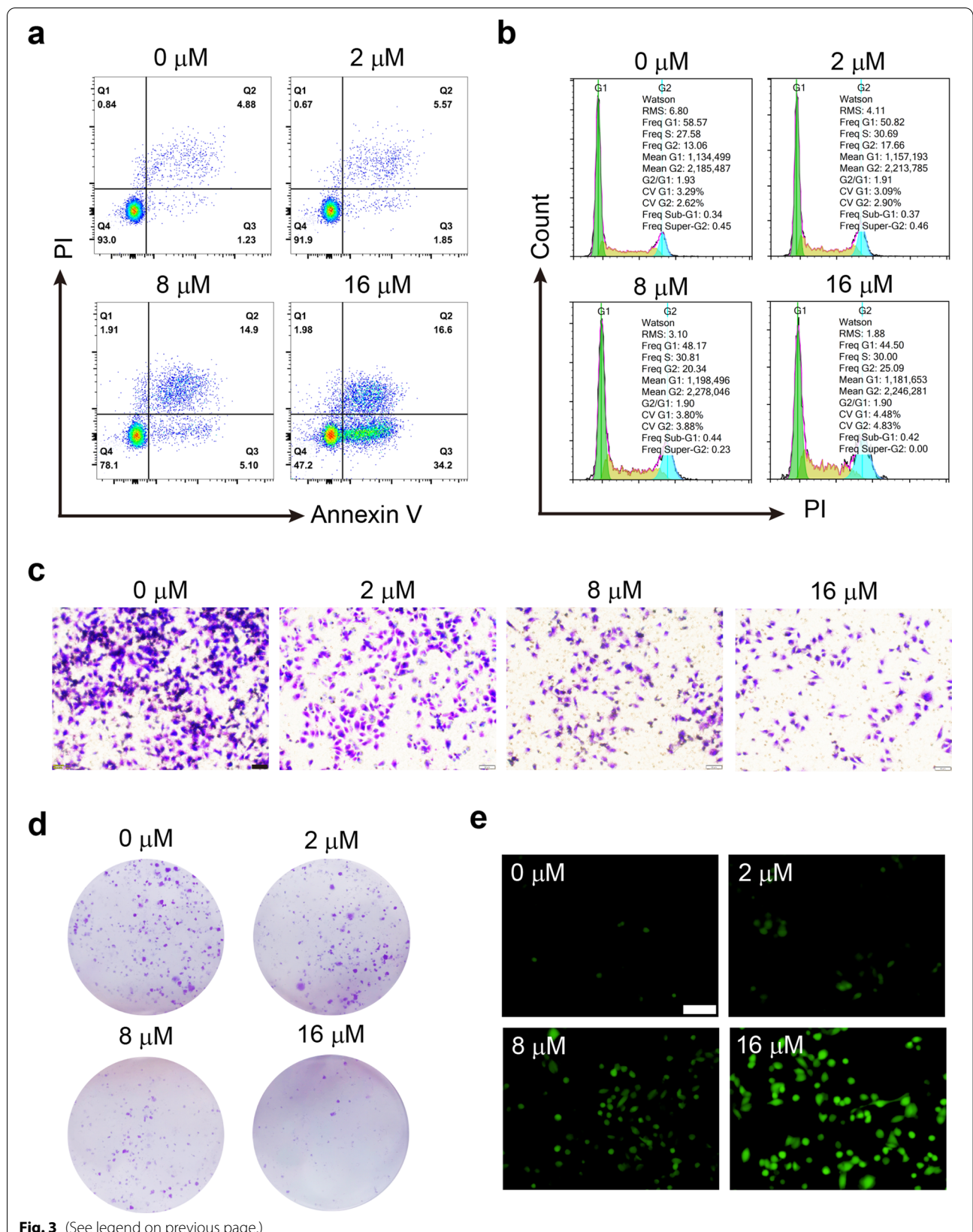


Fig. 3 (See legend on previous page.)

cell survival fraction obviously decreased with the addition of Cu₆NC. In the 16 μM group, even almost no colonies appeared, indicating that Cu₆NC was excellent for CDT.

Cu₆NC induced considerable oxidative stress in vitro, leading to a specific tumor killing effect. Since ROS was detected during EPR test, we explored the underlying mechanisms of Cu₆NC for CDT and detected the intracellular ROS by the probe DCFH-DA, which displayed green fluorescence upon oxidation by ROS. For A375 cells exposed to Cu₆NC 12 h, the observed green fluorescence intensity was enhanced with the increasing of concentration (Fig. 3e and Additional file 1: Fig. S22), suggesting production of ROS via Cu⁺-mediated Fenton reaction. In addition, by detecting the production of ROS in A375 cells at different time points (Additional file 1: Fig. S23), it was shown that Cu₆NC could slowly and sustainably release ROS for at least 48 h. Moreover, we found that the ratio of GSH/GSSG in A375 cells treated with Cu₆NC for 6 h was significantly reduced in a concentration-dependent manner (Additional file 1: Fig. S24), which also indicated that the higher intracellular GSH levels in tumor cells could also be one of the possible mechanisms.

As a transition metal element and also an essential trace element for human, copper has been widely researched for its chemodynamic potential in cancer therapy [46]. Since tumor microenvironment has weakly acidic pH, low oxygen, and high glutathione, once chemodynamic properties enter such environment, chemodynamic cancer therapy is activated via its interaction with glutathione and reinforced by H₂O₂ through release of ROS [47]. Cu₆NC synthesized in this work is an ideal property for chemodynamic cancer therapy. On one hand, the materials characterization results showed that Cu₆NC triggers Fenton-like reaction and generates ROS which the standard mechanism of CDT, indicating its chemodynamic performance to explain its cytotoxicity to cancer cells over normal cells. On the other hand, our biomedical assay reveals that cancer cells treated with Cu₆NC were observed with a higher level of ROS generation and lower GSH/GSSG ratio, showing that chemodynamic cancer therapy is a mechanism of Cu₆NC to treat cancer cells. Therefore, our results confirmed that

Cu₆NC holds a chemodynamic property with potential for the treatment of cancer.

In vivo cancer therapy

Inspired by the good in vitro CDT efficacy, tumor formation assay was performed in vivo by using human melanoma A375 tumor-bearing mice model. Mice with tumors of about 100 mm³ were randomly divided into three groups: (1) Control group, (2) Cu₆NC group (10 mg/kg), and (3) Cu₆NC group (20 mg/kg). According to the corresponding dose of each group, Cu₆NC was administered intraperitoneally every 2 days. The tumor volume was measured every other day (Fig. 4a, b). At the time of final harvest, the tumor volume in the control group increased rapidly, while in the dose of 20 mg/kg group the tumor volume was markedly reduced by about 4.5 times (compared with the control group). Besides, the measured tumor weight also decreased significantly with the increase of the treatment dose (Fig. 4d). To verify the inhibitory effect of Cu₆NC, the proliferation and apoptosis in tumor tissues from each group were further detected. According to the immunohistochemical staining, the Ki67 protein level of the Cu₆NC treatment group was significantly lower than that of the control group (Fig. 4c, e). Consistently, the TUNEL staining also demonstrated a promotion with the increase of the administration concentration (Fig. 4c, f), further proving the ability of Cu₆NC to induce apoptosis.

To evaluate the in vivo biocompatibility of Cu₆NC, the main organs and peripheral blood of the mice were investigated after the mice were sacrificed. Specifically, H&E staining results of the mice in every group showed that no major pathological abnormalities was induced in main organs of mice (Fig. 4g). Concomitantly, none of cardiotoxicity, kidney toxicity or liver toxicity from Cu₆NC was observed in the blood samples (Additional file 1: Fig. S25), indicating the low in vivo toxicity of Cu₆NC.

Therefore, the results confirmed that the mechanism of Cu₆NC for cancer therapy includes CDT, where the break of Cu₆NC generate ROS which plays a role in killing cancer cells [48]. Unlike many previous copper nanoparticles for CDT use where their structure is not atomically precise or with continuous release of ROS, Cu₆NC demonstrates its strong strength in further clinical application

(See figure on next page.)

Fig. 4 In vivo cancer chemotherapy results of Cu₆NC. All mice were randomly divided into 3 groups: normal control group (Control), Cu₆NC group (10 mg/kg), and Cu₆NC group (20 mg/kg), at the same time, were treated by intraperitoneal injection of the corresponding dose of Cu₆NC. **a** Photographs of mice after 16 days of different formulations. **b** Tumor growth curves of mice in different treatment groups. **c** Ki67 staining and TUNEL staining of tumor sections from different treatment groups. Scale bar: 100 μm. **d** Comparison of tumor weight in mice after therapy. The quantitative analysis of Ki67 **e** and TUNEL **f** performed by Image J software. **g** Pathological analysis of various organs in mice injected with different formulations. Scale bar: 50 μm

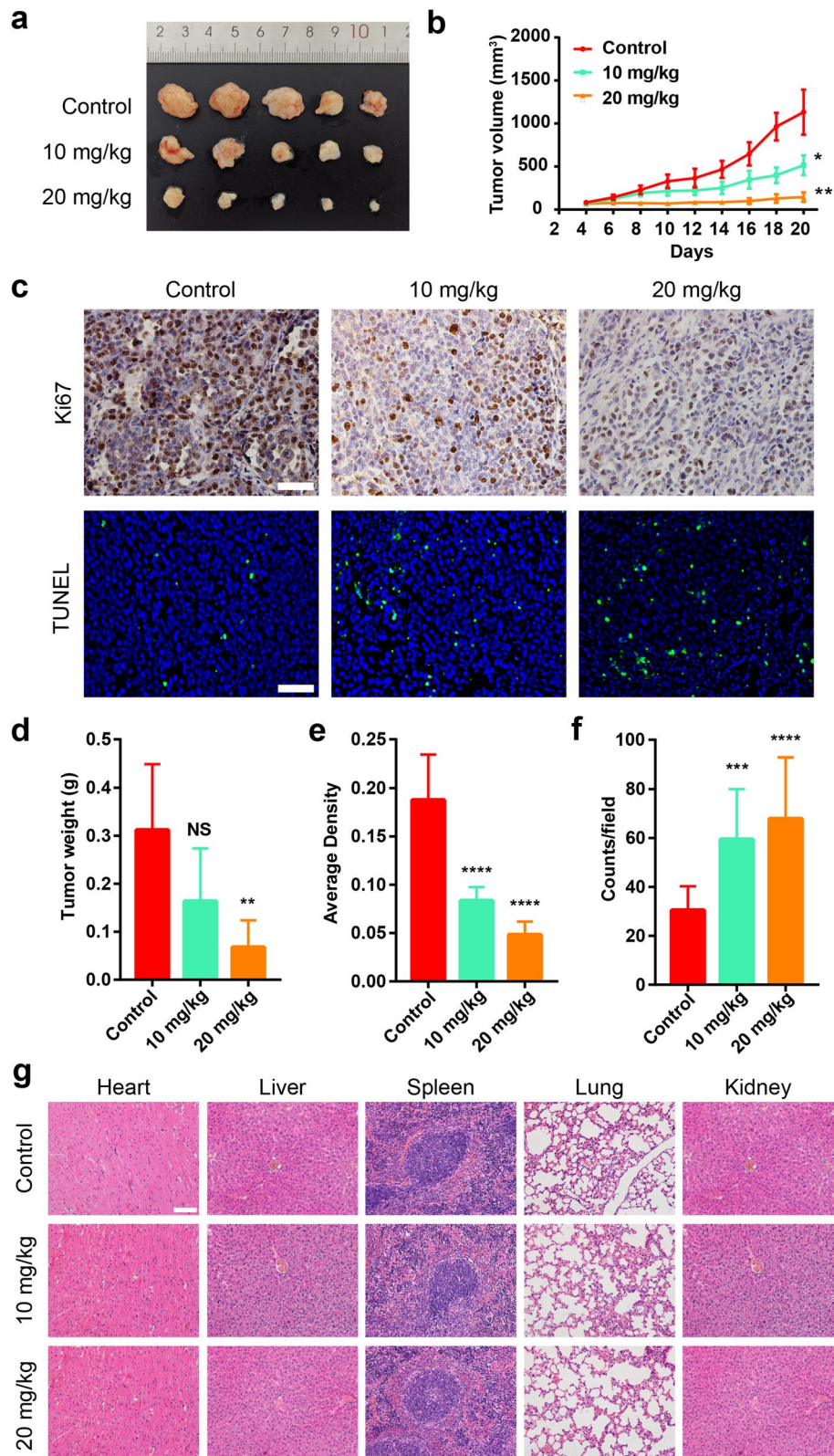


Fig. 4 (See legend on previous page.)

due to its unusual chemodynamic mechanism [49, 50]. Firstly, Cu₆NC is with atomically precise structure that its detection, application and possible side effects once for clinical use can be precisely examined, where there is not uncertain components or allotropic substances existing which may cause unpredictable danger. Secondly, Cu₆NC does not break to generate ROS under environment of normal tissues and is with minor harm to normal tissues which has been tested both in vitro and in vivo, which guaranteed its bio-safety where normal tissues and important organs are not damaged heavily. More importantly, the generation of ROS requires Cu₆NC to interact with tumor microenvironment and break, which means it only works when getting close to cancer cells. Since Cu₆NC is made of copper element which is an essential trace element and a ligand which has been tested to be with high biocompatibility, it breaks to unharmed components after its chemodynamic cancer therapy with cancer cells which further minimize the potential danger in clinical use.

Conclusions

ROS are unstable oxygen containing species, which make it difficult to be persistently subsistent and effective in clinical treatment. On the other hand, lacking of natural targeted properties, the surplus ROS are harmful to normal cells, generating damages or carcinogenesis. In this study, we designed and prepared Cu₆NC with atomically precise structures of Cu₆(C₄H₃N₂S)₆, which could generate large amount of ROS in acidic environment. Such characters address the above conundrum: (1) Cu₆NC could slowly degrade and sustainably release ROS; (2) the fragmentation of Cu₆NC are induced under acidic environment, providing targeted properties. Thus, Cu₆NC could be fragmented under the acidic tumor microenvironment with sustainable burst of ROS. Both in vitro and in vivo experiments confirm that Cu₆NC not only present high cytotoxicity to tumor cells, but also ensure the biological safety. Our intelligent strategy not only develops a promising candidate for the targeted CDT of cancer cells, but also paves the way for addressing clinical issues at the atomic level.

Experimental section

Synthesis of Cu₆(C₄H₃N₂S)₆

2-Mercaptopyrimidine ($\geq 99\%$) was purchased from Alfa Aesar. N,N-dimethylformamide (DMF) and Copper nitrate trihydrate(II) (Cu(NO₃)₂·3H₂O, $\geq 99\%$) were bought from Sinopharm Chemical Reagent Co., Ltd., China. All reagents and solvents used were of commercially

available reagent grade and used without further purification. 2-Mercaptopyrimidine (112 mg, 1 mmol) and Cu(NO₃)₂·3H₂O (240 mg, 1 mmol) were dissolved in 20 ml DMF solution respectively, stir thoroughly to dissolve completely. Subsequently, add the DMF solution of 2-Mercaptopyrimidine dropwise to the solvent of Cu(NO₃)₂·3H₂O. Cu₆L₆ powder crystals (C₂₄H₁₈Cu₆N₁₂S₆) were obtained by filtration after vigorous stirring at room temperature for 2 h (a single crystal suitable for SCXRD measurements can be obtained by reducing the dosage in the same proportion).

Characterization

Powder X-ray diffraction (PXRD) patterns of the samples were acquired on a Rigaku D/Max-2500PC X-ray diffractometer with Cu radiation ($\lambda = 1.54178 \text{ \AA}$). Fourier transform infrared (FT-IR) spectroscopy was conducted using a Bruker ALPHA II FT-IR spectrometer. X-ray photoelectron spectroscopy (XPS) analysis was obtained on an ESCALAB 250 instrument operated at 150 W and 200 eV with mono chromated Al K α radiation. Thermogravimetric analyses (TGA) were performed on an SDT 2960 thermal analyzer from room temperature (RT) to 800 °C at a heating rate of 10 °C/min under a nitrogen atmosphere. Dynamic light scattering (DLS) data were obtained by Horiba nano Partica SZ-100V2. UV-vis absorption spectra were recorded using a Hitachi UH4150 UV-visible spectrophotometer in the range of 200–700 nm. Emission and excitation spectra at RT were recorded with an Edinburgh FLS 1000 fluorescence spectrometer, and luminescence microscopy images were recorded on an Olympus BX53 microscope. Electron paramagnetic resonance (EPR) spectra were recorded by a Bruker A 300 EPR spectrometer.

Single-crystal X-ray diffraction (SCXRD) analysis

SCXRD was performed on a Rigaku XtaLAB Pro diffractometer Cu-K α radiation ($\lambda = 1.54184 \text{ \AA}$) at 200 K. Data collection and reduction were conducted with CrysAlis-Pro software. The structures were solved with intrinsic phasing methods (SHELXT-2015) and refined by full-matrix least-squares on F₂ using OLEX2, which utilizes the SHELXL-2015 module. The imposed restraints in least-squares refinement of each structure were commented in the corresponding CIF files. All non-hydrogen atoms were refined anisotropically, and the hydrogen atoms were included in idealized positions. The crystal structures are visualized by DIAMOND 3.2. The detailed information of the crystal data, data collection and refinement results are summarized in Additional file 1: Table S1.

Fenton-like reaction

The colorimetric method was used to analyze the absorbance change of methylene blue (MB), indicating that $\cdot\text{OH}$ is produced. Solutions of 25 mg/L MB, 10 mM H_2O_2 , and 0.1 mM Cu_6NC were formed at different pH values. After 2 h of incubation, the color changes of the solution were obtained.

Cell culture

Cell lines including human melanoma cells (A375), human esophageal cancer cells (Kyse30), human breast cancer cells (MCF-7) and Rat cardiomyocytes cells (H9C2) were purchased from the cell bank of the Chinese Academy of Sciences (Shanghai, China). A375 and H9C2 cells were cultured in DMEM medium containing 10% FBS and 1% penicillin–streptomycin. MCF-7 and Kyse30 cells incubated in 1640 medium containing 10% FBS and 1% penicillin–streptomycin.

Cytotoxicity analysis

A375, MCF-7 and Kyse30 cells were seeded in 96-well plates (8×10^3 cells per well), respectively, and cultured for overnight. Then these cells were incubated with different concentrations of Cu_6NC (0, 2, 4, 8, 12, 15, 20 and 25 μM), the incubation time was 24 h and 48 h, respectively. Finally, add 10 μL of CCK-8 solution to each well and incubate for another 1 h. The absorbance of cells in each well at 450 nm was measured by a microplate reader. The cytotoxicity test of Cu_6NC on H9C2 cells was also carried out according to the above description. Correspondingly, the toxicity of the pure ligand to A375 cells was tested with CCK-8.

Cellular uptake of Cu_6NC

A375 and H9C2 cells were seeded in culture dishes and incubated for 24 h. Subsequently, cells were incubated with 8 μM Cu_6NC and harvested after 3 h and 6 h. The percentage of positive cells was tested by the flow cytometry (ACEA NovoCyte3130, USA) with an excitation wavelength of 405 nm and an emission wavelength of 780 nm. Data were processed by FlowJo software.

Apoptosis and cell cycle analysis

A375 (2.5×10^5 cells per well) cells were seeded in 6-well plates with 0, 2, 8 and 16 μM Cu_6NC for 24 h. The cells were collected using trypsin–EDTA and stained with annexin V-FITC/PI (BD Biosciences, USA) for 15 min, and then apoptotic cells were identified by flow cytometry. The cell cycle was measured by PI staining using a cell cycle analysis kit (KeyGen Biotech, China). After staining following the manufacturer's instructions, the cells were

analyzed by flow cytometry (FACS Aria III, USA). Data were processed by ModFit LT software.

Cell dead/live assay

A375 cells were treated with Cu_6NC (0, 2, 8 and 16 μM) for 24 h. Before being observed with a fluorescence microscope, the cells were washed twice with PBS and incubated with 2 μM calcein AM and 4.5 μM PI for 20 min. For flow cytometry detection, after being digested and harvested, the cells are washed twice by PBS and then tested by a FACS Aria III flow cytometer. Data were processed and analyzed by FlowJo software.

Transwell migration assay

Migration assays of A375 in vitro were performed using a 24-well plate with a transwell polycarbonate permeable support (pore size, 8 μm ; Corning Incorporated, Corning, USA). A375 cells were incubated and treated as described in the Apoptosis Assay. The harvested cells were resuspended in FBS-free medium and seeded in the upper chamber with 1×10^5 cells per well. The lower chamber was filled with 20% FBS medium (600 μL /well). The cells were then cultured for 48 h. Finally, the cells in the lower layer of the upper chambers were fixed with 4% paraformaldehyde and stained with 0.1% crystal violet. Numbers of migrated cells were photographed with a fluorescence microscopy and processed by ImageJ software.

Colony formation ability identification

A375 cells were incubated and treated as described in the Apoptosis Assay. The cells were digested and seeded in 6-well plates (1000 cells per well). Then the cells are cultured in complete medium, and the medium was changed every 4 days. At 12 days, the cells were fixed with 4% paraformaldehyde and stained with 0.1% crystal violet. The cell colonies were observed and photographed with a microscope, and the colonies containing more than 50 cells were counted using ImageJ software.

Intracellular reactive oxygen species (ROS) generation

A375 cells (5×10^4 cells/well) were incubated in a 24-well plate with different concentrations of Cu_6NC (0, 2, 8 and 16 μM) for 12 h. Then, the level of cellular ROS was measured by 2',7-dichlorodihydrofluorescein diacetate (DCFH-DA) probe (Beyotime Biotechnology, Jiangsu, China). Firstly, the cells were washed twice with PBS, incubated with DCFH-DA (10 μM) for 25 min, and then washed with PBS three times. Finally, the ROS signal of the cells was observed by a fluorescence microscopy. In addition, according to the above method, the production

of ROS in A375 cells after 8 μM Cu_6NC treatment was detected at different times (0, 2, 4, 8, 12, 24, 36 and 48 h).

Assessment of glutathione (GSH)

Levels of GSH in A375 cells after treatment with Cu_6NC were evaluated with GSH and GSSG assay kits (Beyotime Biotechnology, Jiangsu, China). In short, A375 cells were seeded in 6-well dishes (2×10^5 cells per well) and treated with different concentrations of Cu_6NC (0, 2, 8 and 16 μM) for 6 h. Then, the cells were collected with centrifugation, and the supernatant was discarded. Samples were added protein remover M (10 mg/30 μL), subjected to 3 cycles of freezing–thawing, and then centrifugated at 1000g for 10 min at 4 °C. The supernatant was reserved for GSH measurement with GSH and GSSG assay kits according to the manufacturer's protocol.

In vivo chemodynamic therapy

All animal procedures were conducted in accordance with the Guide for the Care and Use of Laboratory Animals and were approved by the Welfare and Ethics Review Committee of Zhengzhou University Laboratory Animal Center (Approval number: ZZU-LAC20200911[14]). In order to generate a xenograft mouse model, on day 0, we planted A375 cells (5×10^6 tumor cells in 200 μL of PBS) in 6-week-old female BALB/c nude mice (Beijing Vital River Laboratory Animal Technology Co. Ltd, China) subcutaneously in the right flank. When the tumor volume reached about 100 mm^3 on the 4th day, we randomly divided the mice into three groups: normal control group (Control), Cu_6NC group (10 mg/kg), and Cu_6NC group (20 mg/kg), at the same time by intraperitoneal injection corresponding dose of Cu_6NC to treat mice. Mice were exposed to these treatments every other day for a total of nine administrations. The length (L) and width (W) of the tumor were measured with a vernier caliper every 2 days, and the tumor volume (V) was calculated using the formula: $V = L \times W^2/2$. On the 20th day, the tumor tissues, peripheral blood, and major organs (heart, liver, spleen, lungs and kidneys) of mice were harvested.

All harvested tissues were fixed with 4% formalin at least for 48 h. The fixed tissues were used for experiments such as hematoxylin and eosin (H&E) and immunohistochemistry staining. Apoptosis of tumor tissue sections was detected by staining with terminal deoxynucleotidyl transferase dUTP nick end labeling (TUNEL). The proliferation of tumor tissue was detected by immunohistochemical Ki67 staining. H&E were used to stain sections of major organs in each group. All these stained sections could be observed with a fluorescence microscopy. After the peripheral blood was collected, a serum sample was obtained by centrifugation. Then, an automatic biochemical analyzer (Chemray 240 or 840, Rayto, China) was

used to detect the indexes of liver function, kidney function and myocardial enzymes.

Statistical analysis

All results are presented as the mean \pm standard deviation (SD). Two treatment groups were compared by Student's t test. Multiple group comparisons were performed by two-way analysis of variance with Tukey's post hoc test. All statistical analyses were carried out using GraphPad Prism 5. * $p < 0.05$, ** $p < 0.01$, *** $p < 0.001$ and **** $p < 0.0001$ were deemed as significant differences. "NS" indicates no significant differences.

Supplementary Information

The online version contains supplementary material available at <https://doi.org/10.1186/s12951-021-01207-6>.

Additional file 1. Additional table and figures.

Acknowledgements

The authors greatly appreciate the financial support from the National Science Fund for Distinguished Young Scholars (No. 21825106) and the National Natural Science Foundation of China (Nos. 22005273 and 802073168).

Authors' contributions

PP, BL and SZ conceived various aspects of the project. ZY and AY performed all experiments on synthesis and characterize of metal nanoclusters, in vitro and in vivo experiments, data collection and analysis. WM, KM and YL performed experiments on chemical and morphological characterizations of nanoclusters and worked on data analysis. PP and ZY wrote the manuscript with input from other authors. ZY and AY contributed equally to this work. All authors read and approved the final manuscript.

Availability of data and materials

The datasets supporting the conclusions of this article are included within the article and its additional file.

Declarations

Ethics approval and consent to participate

All animal procedures were conducted in accordance with the Guide for the Care and Use of Laboratory Animals and were approved by the Welfare and Ethics Review Committee of Zhengzhou University Laboratory Animal Center (Approval number: ZZU-LAC20200911[14]).

Consent for publication

All authors consent to publish.

Competing interests

The authors declare that they have no competing interests.

Author details

¹Department of Oncology, The First Affiliated Hospital of Zhengzhou University, Zhengzhou 450052, China. ²Henan Key Laboratory of Crystalline Molecular Functional Materials, Henan International Joint Laboratory of Tumor Theranostical Cluster Materials, Green Catalysis Center, and College of Chemistry, Zhengzhou University, Zhengzhou 450001, China. ³Department of Breast Oncology, State Key Laboratory of Oncology in South China, Collaborative Innovation Center for Cancer Medicine, Sun Yat-sen University Cancer Center, Guangzhou 510060, China.

Received: 31 August 2021 Accepted: 14 December 2021
Published online: 06 January 2022

References

1. Sayin VI, Ibrahim MX, Larsson E, Nilsson JA, Lindahl P, Bergo MO. Antioxidants accelerate lung cancer progression in mice. *Sci Transl Med*. 2014;6:8.
2. Cui Q, Wang JQ, Assaraf YG, Ren L, Gupta P, Wei LY, Ashby CR, Yang DH, Chen ZS. Modulating ROS to overcome multidrug resistance in cancer. *Drug Resist Updates*. 2018;41:1–25.
3. Yu XY, Lao YM, Teng XL, Li S, Zhou Y, Wang FX, Guo XW, Deng SY, Chang YZ, Wu XF, Liu ZD, Chen L, Lu LM, Cheng JK, Li B, Su B, Jiang J, Li HB, Huang CX, Yi J, Zou Q. SENP3 maintains the stability and function of regulatory T cells via BACH2 deSUMOylation. *Nat Commun*. 2018;9:11.
4. De Nicola GM, Kareth FA, Humpton TJ, Gopinathan A, Wei C, Frese K, Mangal D, Yu KH, Yeo CJ, Calhoun ES, Scrimieri F, Winter JM, Hruban RH, Iacobuzio-Donahue C, Kern SE, Blair IA, Tuveson DA. Oncogene-induced Nrf2 transcription promotes ROS detoxification and tumorigenesis. *Nature*. 2011;475:106–U128.
5. Lu Y, Chen B, Song JH, Zhen T, Wang BY, Li X, Liu P, Yang X, Zhang QL, Xi XD, Chen SD, Zuo JP, Chen Z, Chen SJ. Eriocalyxin B ameliorates experimental autoimmune encephalomyelitis by suppressing Th1 and Th17 cells. *Proc Natl Acad Sci USA*. 2013;110:2258–63.
6. Hultqvist M, Olofsson P, Gelderman KA, Holmberg J, Holmdahl R. A new arthritis therapy with oxidative burst inducers. *PLoS Med*. 2006;3:1625–36.
7. Chen X, Stewart E, Shelat AA, Qu CX, Bahrami A, Hatley M, Wu G, Bradley C, McEvoy J, Pappo A, Spunt S, Valentine MB, Valentine V, Krafcik F, Lang WH, Wierdl M, Tsurkan L, Tolleman V, Federico SM, Morton C, Lu C, Ding L, Easton J, Rusch M, Nagahawatte P, Wang JM, Parker M, Wei L, Hedlund E, Finkelstein D, Edmonson M, Shurtleff S, Boggs K, Mulder H, Yergeau AM, Skapek S, Hawkins DS, Ramirez N, Potter PM, Sandoval JA, Davidoff AD, Mardis ER, Wilson RK, Zhang JH, Downing JR, Dyer MA, St Jude Childrens Res H. Targeting oxidative stress in embryonal rhabdomyosarcoma. *Cancer Cell*. 2013;24:710–24.
8. Love NR, Chen YY, Ishibashi S, Kritsiligkou P, Lea R, Koh Y, Gallop JL, Dorey K, Amaya E. Amputation-induced reactive oxygen species are required for successful *Xenopus* tadpole tail regeneration. *Nat Cell Biol*. 2013;15:222–8.
9. Gauron C, Rampon C, Bouzaffour M, Ipendey E, Teillon J, Volovitch M, Vriz S. Sustained production of ROS triggers compensatory proliferation and is required for regeneration to proceed. *Sci Rep*. 2013;3:9.
10. Kleinauskas A, Rocha S, Sahu S, Sun YP, Juzenas P. Carbon-core silver-shell nanodots as sensitizers for phototherapy and radiotherapy. *Nanotechnology*. 2013;24:10.
11. Goswami N, Luo ZT, Yuan X, Leong DT, Xie JP. Engineering gold-based radiosensitizers for cancer radiotherapy. *Mater Horizons*. 2017;4:817–31.
12. Su X-Y, Liu P-D, Wu H, Gu N. Enhancement of radiosensitization by metal-based nanoparticles in cancer radiation therapy. *Cancer Biol Med*. 2014;11:86–91.
13. Jin RC, Zeng CJ, Zhou M, Chen YX. Atomically precise colloidal metal nanoclusters and nanoparticles: fundamentals and opportunities. *Chem Rev*. 2016;116:10346–413.
14. Chakraborty I, Pradeep T. Atomically precise clusters of noble metals: emerging link between atoms and nanoparticles. *Chem Rev*. 2017;117:8208–71.
15. Ghosh A, Mohammed OF, Bake OM. Atomic-level doping of metal clusters. *Acc Chem Res*. 2018;51:3094–103.
16. Naatz H, Manshian BB, Rios Lucí C, Tsikourkitoudi V, Deligiannakis Y, Birkentstock J, Pokhrel S, Madler L, Soenen SJ. Model-based nanoengineered pharmacokinetics of iron-doped copper oxide for nanomedical applications. *Angew Chem*. 2020;59:1828–36.
17. Sharma S, Chakrahari KK, Saillard JY, Liu CW. Structurally Precise Dichalcogenolate-Protected Copper and Silver Superatomic Nanoclusters and Their Alloys. *Acc Chem Res*. 2018;51:2475–83.
18. Lei Z, Wan XK, Yuan SF, Guan ZJ, Wang QM. Alkynyl approach toward the protection of metal nanoclusters. *Acc Chem Res*. 2018;51:2465–74.
19. Sakhivel NA, Dass A. Aromatic thiolate-protected series of gold nanomolecules and a contrary structural trend in size evolution. *Acc Chem Res*. 2018;51:1774–83.
20. Kwak K, Lee D. Electrochemistry of atomically precise metal nanoclusters. *Acc Chem Res*. 2019;52:12–22.
21. Tang Q, Hu GX, Fung V, Jiang DE. Insights into interfaces, stability, electronic properties, and catalytic activities of atomically precise metal nanoclusters from first principles. *Acc Chem Res*. 2018;51:2793–802.
22. Jiang XY, Du BJ, Zheng J. Glutathione-mediated biotransformation in the liver modulates nanoparticle transport. *Nat Nanotechnol*. 2019;14:874.
23. Chakraborty P, Nag A, Chakraborty A, Pradeep T. Approaching materials with atomic precision using supramolecular cluster assemblies. *Acc Chem Res*. 2019;52:2–11.
24. Nonappa IO. Hydrogen bonding directed colloidal self-assembly of nanoparticles into 2D crystals, capsids, and supracolloidal assemblies. *Adv Funct Mater*. 2018;28:14.
25. Zhang XD, Luo ZT, Chen J, Shen X, Song SS, Sun YM, Fan SJ, Fan FY, Leong DT, Xie JP. Ultrasmall Au_{10–12}(SG)(10–12) nanomolecules for high tumor specificity and cancer radiotherapy. *Adv Mater*. 2014;26:4565.
26. Liang GH, Jin XD, Zhang SX, Xing D. RGD peptide-modified fluorescent gold nanoclusters as highly efficient tumor-targeted radiotherapy sensitizers. *Biomaterials*. 2017;144:95–104.
27. Chen Q, Chen JW, Yang ZJ, Xu J, Xu LG, Liang C, Han X, Liu Z. Nanoparticle-enhanced radiotherapy to trigger robust cancer immunotherapy. *Adv Mater*. 2019;31:12.
28. Yi X, Chen L, Chen J, Maiti D, Chai ZF, Liu Z, Yang K. Biomimetic copper sulfide for chemo-radiotherapy: enhanced uptake and reduced efflux of nanoparticles for tumor cells under ionizing radiation. *Adv Funct Mater*. 2018;28:11.
29. Juzenas P, Chen W, Sun YP, Coelho MAN, Generalov R, Generalova N, Christensen IL. Quantum dots and nanoparticles for photodynamic and radiation therapies of cancer. *Adv Drug Deliv Rev*. 2008;60:1600–14.
30. Ghahremani F, Kefayat A, Shahbazi-Gahrouei D, Motaghi H, Mehrgardi MA, Haghjooy-Javanmard S. AS1411 aptamer-targeted gold nanoclusters effect on the enhancement of radiation therapy efficacy in breast tumor-bearing mice. *Nanomedicine*. 2018;13:2563–78.
31. Li B, Lv Y-K, Wang Z-D, Peng P, Zang S-Q. Edge confined covalent organic framework with efficient biocompatibility and photothermic conversion. *Nano Today*. 2021;37:101101.
32. Zhang MM, Dong XY, Wang ZY, Li HY, Li SJ, Zhao XL, Zang SQ. AIE triggers the circularly polarized luminescence of atomically precise enantiomeric copper(I) alkynyl clusters. *Angew Chem-Int Ed*. 2020;59:10052–8.
33. Huang JH, Wang ZY, Zang SQ, Mak TCW. Spontaneous resolution of chiral multi-thiolate-protected Ag-30 nanoclusters. *ACS Central Sci*. 2020;6:1971–6.
34. Li HY, Zhao SN, Zang SQ, Li J. Functional metal-organic frameworks as effective sensors of gases and volatile compounds. *Chem Soc Rev*. 2020;49:6364–401.
35. Han Z, Zhao XL, Peng P, Li S, Zhang C, Cao M, Li K, Wang ZY, Zang SQ. Intercluster aurophilicity-driven aggregation lighting circularly polarized luminescence of chiral gold clusters. *Nano Res*. 2020;13:3248–52.
36. Dong XY, Si YB, Yang JS, Zhang C, Han Z, Luo P, Wang ZY, Zang SQ, Mak TCW. Ligand engineering to achieve enhanced ratiometric oxygen sensing in a silver cluster-based metal-organic framework. *Nat Commun*. 2020;11:9.
37. Kong YJ, Yan ZP, Li S, Su HF, Li K, Zheng YX, Zang SQ. Photoresponsive propeller-like chiral AIE copper(I) clusters. *Angew Chem-Int Ed*. 2020;59:5336–40.
38. Jin Y, Li S, Han Z, Yan BJ, Li HY, Dong XY, Zang SQ. Cations controlling the chiral assembly of luminescent atomically precise copper(I) clusters. *Angew Chem-Int Ed*. 2019;58:12143–8.
39. Huang Q, Zhang SH, Zhang H, Han YB, Liu HH, Ren F, Sun Q, Li Z, Gao MY. Boosting the radiosensitizing and photothermal performance of Cu₂-xSe nanocrystals for synergetic radiophotothermal therapy of orthotopic breast cancer. *ACS Nano*. 2019;13:1342–53.
40. Jin Y, Zhang C, Dong XY, Zang SQ, Mak TCW. Shell engineering to achieve modification and assembly of atomically-precise silver clusters. *Chem Soc Rev*. 2021;50:2297–319.
41. Hu K, Xie L, Zhang YD, Hanyu M, Yang ZM, Nagatsu K, Suzuki H, Ouyang J, Ji XY, Wei JJ, Xu H, Farokhzad OC, Liang SH, Wang L, Tao W, Zhang MR. Marriage of black phosphorus and Cu²⁺ as effective photothermal agents for PET-guided combination cancer therapy. *Nat Commun*. 2020;11:1:15.
42. Liu Y, Wu JD, Jin YH, Zhen WY, Wang YH, Liu JH, Jin LH, Zhang ST, Zhao Y, Song SY, Yang Y, Zhang HJ. Copper(I) phosphide nanocrystals for in situ self-generation magnetic resonance imaging-guided photothermal-enhanced chemodynamic synergetic therapy resisting deep-seated tumor. *Adv Funct Mater*. 2019;29:8.

43. Zhou RS, Zhang XY, Fu J, Xin LD, Jiao WZ, Song JF. Four new Cu₆S₆ cluster-based coordination compounds: synthesis, crystal structures and fluorescence properties. *Dalton Trans.* 2021;50:4567–76.
44. Kolosenko I, Avnet S, Baldini N, Viklund J, De Milito A. Therapeutic implications of tumor interstitial acidification. *Semin Cancer Biol.* 2017;43:119–33.
45. Rohani N, Hao L, Alexis MS, Joughin BA, Krismer K, Moufarrej MN, Soltis AR, Lauffenburger DA, Yaffe MB, Burge CB, Bhatia SN, Gertler FB. Acidification of tumor at stromal boundaries drives transcriptome alterations associated with aggressive phenotypes. *Can Res.* 2019;79:1952–66.
46. Hao YN, Zhang WX, Gao YR, Wei YN, Shu Y, Wang JH. State-of-the-art advances of copper-based nanostructures in the enhancement of chemodynamic therapy. *J Mater Chem B.* 2021;9:250–66.
47. Ma B, Wang S, Liu F, Zhang S, Duan J, Li Z, Kong Y, Sang Y, Liu H, Bu W, Li L. Self-Assembled copper-amino acid nanoparticles for in situ glutathione "AND" H₂O₂ sequentially triggered chemodynamic therapy. *J Am Chem Soc.* 2019;141:849–57.
48. Liu C, Wang D, Zhang S, Cheng Y, Yang F, Xing Y, Xu T, Dong H, Zhang X. Biodegradable biomimic copper/manganese silicate nanospheres for chemodynamic/photodynamic synergistic therapy with simultaneous glutathione depletion and hypoxia relief. *ACS Nano.* 2019;13:4267–77.
49. Wang L, Zhang Z, Ding Y, Wu J, Hu Y, Yuan A. Novel copper-based and pH-sensitive nanomedicine for enhanced chemodynamic therapy. *Chem Commun.* 2020;56:7753–6.
50. Zhao Y, Chen BQ, Kankala RK, Wang SB, Chen AZ. Recent advances in combination of copper chalcogenide-based photothermal and reactive oxygen species-related therapies. *ACS Biomater Sci Eng.* 2020;6:4799–815.

Publisher's Note

Springer Nature remains neutral with regard to jurisdictional claims in published maps and institutional affiliations.

Ready to submit your research? Choose BMC and benefit from:

- fast, convenient online submission
- thorough peer review by experienced researchers in your field
- rapid publication on acceptance
- support for research data, including large and complex data types
- gold Open Access which fosters wider collaboration and increased citations
- maximum visibility for your research: over 100M website views per year

At BMC, research is always in progress.

Learn more biomedcentral.com/submissions

